Journal of Thermal Science Vol.32, No.4 (2023) 1321−1334

https://doi.org/10.1007/s11630-023-1836-5 **Article ID: 1003-2169(2023)04-1321-14**

Design Optimization of Non-Axisymmetric Vane for an Axial Compressor under Inlet Distortion

ZHANG Min[1,2,3,4], DU Juan[1,2,3,4*], ZHAO Hongliang[1,2,3,4], QIU Jiahui[1,2,3,4], BA Dun[1,2,3,4], CHEN Yang[1,2,3,4], NIE Chaoqun[1,2,3,4]

1. Digital Twin Research Center, Institute of Engineering Thermophysics, Chinese Academy of Sciences, Beijing 100190, China
2. Key Laboratory of Advanced Energy and Power, Chinese Academy of Sciences, Beijing 100190, China
3. Innovation Academy for Light-Duty Gas Turbine, Chinese Academy of Sciences, Beijing 100190, China
4. School of Engineering Science, University of Chinese Academy of Sciences, Beijing 100049, China

Abstract: The flow field at the inlet of compressors is generally encountered combined total pressure and swirl distortion for either aircraft engine with S-duct or gas turbine with lateral air intake. This inevitably deteriorates compressor aerodynamic performance, including not only the efficiency or pressure ratio but also the operation stability. In order to conquer this issue, appropriate measures such as integrating flow control techniques and modifying inlet or compressor design are of benefits. Due to this motivation, this article develops a full-annular two-dimensional (2D) and a partial-annular three-dimension (3D) optimization strategy for non-axisymmetric vane design. Firstly, two numerical simulation methods for evaluating performance of full-annular 2D vane and compressor with partial-annular 3D vane are developed. The swirl patterns at the inlet of a 1.5-stage axial compressor are analyzed and parametrized, and the parameterization is transferred to characterize the circumferential distribution of geometrical parameters of the vane profile. These approaches dramatically reduce computational simulation costs without violating the non-axisymmetric flow distortion patterns. Then various full-annular 2D sections at different radial locations are constructed as design space. The designed vane is reconstructed and 3D numerical simulations are performed to examine performance of the non-axisymmetric vane and the compressor with it. Also, partial annular 3D optimization is conducted for balancing compressor efficiency and stall margin. Results indicate that the designed non-axisymmetric vane based on full-annular optimization approach can decrease the vane total pressure loss under the considered inlet flow distortion, while those using partial-annular optimization achieve positive effects on compressor stall margin.

Keywords: combined total pressure and swirl distortion, axial compressor, non-axisymmetric vane, optimization, aerodynamic performance

Received: Mar 28, 2023 AE: ZHANG Hongwu Corresponding author: DU Juan E-mail: dujuan@iet.cn

www.springerlink.com

Nomenclature

b	Blade chord/mm	θ	Coordinate axis/mm
c_k	Amplitude of Fourier coefficients	π	Pressure ratio
IGV	Inlet guide vane	φ_k	Phase of Fourier coefficients
i_{ax}	Axial momentum	χ_1	Leading edge metal angle
$i_{ax,c}$	Accumulated axial momentum from blade leading edge	$\chi_{1,dis}$	Inlet angle distortions
$i_{ax,LE}$	Maximum value of $i_{ax,c}$	χ_2	Trailing edge metal angle
m	Mass flow rate/kg·s^{-1}	**Subscripts**	
N	Grid number/blade number	b	blade chord or coefficient
P	Pressure/Pa	d	design
R_n	Span-normalized locations	I	IGV
T	Temperature/K	i,j,k	Coordinate index
TLF	Tip leakage flow	in,out	Inlet and outlet
Δs	entropy change	is	isentropic
t	Blade thickness/mm	n	Normalized
U	Rotating velocity of blade	R	Rotor
V	Velocity	S	Stator
z	Coordinate axis/mm	s	static parameter
α_u	Flow angle/(°)	t	total parameter in absolute coordinate
β	Relative flow angle/(°)	tw	total parameter in relative coordinate
η	Efficiency	F1,F2	Fourier mode number

1. Introduction

Non-uniform flow field is generally inevitable at the inlet of a compressor due to flow separation in S-duct intake [1] or lateral air intake [2] of aircraft engine or gas turbine respectively. Also, its manifestation is often in the form of combined total pressure and swirl distortion. This not only deteriorates the efficiency and pressure ratio of a compressor, but also narrows the compressor stall margin. Therefore, investigating effects of the combined total pressure and swirl inflow on compressor performance is a long-term requirement for modern and next-generation gas turbine engines.

Study on total pressure distortion can ascend to the middle of last century, and one of innovative works was conducted by Pearson and Meckein [3], who first proposed the parallel compressor theory for evaluating compressor performance under total pressure distortion. Later, Reid [4] pointed out that effects of inlet distortion are related to the distortion extent, and hence they defined the concept of critical angle. Based on the internal flow theory, Stenning [5] made an interpretation that the mechanism of decreased stall margin under total pressure distortion lied in the reduced axial velocity, which increased the incidence angle at the blade leading edge and hence strengthened flow separations could induce rotating stall in advance. Based on these cornerstone achievements, modern research scholars carry out more elaborate and advanced experiments or CFD (Computational Fluid Dynamic) simulations to dig out physical mechanism of performance deterioration for compressors under inlet total pressure distortion. Typical discoveries include the advanced spillage of the interface between passage and tip clearance flow [6, 7] and intensified corner separation [8, 9]. Apart from these, swirl distortion received attentions due to the usage of compact S-duct in military aircrafts [10] and boundary layer ingestion fan [11]. Davids et al. [12] from Arnold Engineering Development Center conducted a series of work to analyze the impacts of inlet swirl on a two-stage transonic fan. Their results demonstrated that positive swirl (relative to blade rotating direction, also termed as co-swirl) could reduce the rotor pressure ratio due to the reduction in the blade incidence angle but broaden the compressor stall margin, while the negative swirl (or counter-swirl) led to opposite effects to the co-swirl. Similar results were also obtained in the experiments conducted by Dong et al. [13]. With respect to the combined total pressure and swirl distortion, Davis et al. [14] further conducted a parametric study based on the parallel compressor theory for the same compressor as that in Ref. [12]. They concluded that the combined total pressure and swirl distortion reduced the compressor pressure ratio, and the stall margin was mainly determined by the swirl type (i.e., the low pressure combined with counter-swirl had the widest stall margin, while that

combined co-swirl had the poorest stability performance).

In order to match the inlet swirl distortion, non-axisymmetric vane or stator is proposed and gets attention from research and industrial institutes. Hall [15] studied the effects of non-axisymmetric stator trailing edge angle on the NASA R4 fan under inlet distortion, and pointed out that the non-axisymmetric design could reduce the flow non-uniformity at rotor inlet by 40%–50%. A design procedure for non-axisymmetric stator was established by Gunn and Hall [16], who first adjusted blade leading edge metal angle according to the non-uniform flow, then altered axial chord to ensure the diffusion factor and finally adopted the blade lean technique. The designed non-axisymmetric stator reduced the stator loss by 10%, which corresponded to an improvement in the stage efficiency of 0.3%. In addition, the non-axisymmetric design on the stator of stage 67 compressor carried out by Lu et al. [17] also inhibited the corner separation in the stator passage and achieved an improvement in the efficiency by 0.83%. The above non-axisymmetric design efforts mainly depend on manual adjustment, while the work of Kumar et al. [18] established an optimization system based on CFD simulation and Generic algorithm. Their efforts realized a reduction in flow non-uniformity by 50%. However, the optimization cost was relatively huge as unsteady full-annular simulations were employed during the whole design process.

Based on the above literature review, the authors notice that there are two issues that need further investigation. The first is that optimization method with less computation cost is still worth developing for industrial application of the non-axisymmetric design. Secondly, compressor efficiency and stall margin are rarely considered during the optimization or design stage. Due to these considerations and according to a mission requirement of performance improvement for the compressor in an industrial gas turbine, the present article aims to develop a design optimization method of non-axisymmetric vane to match inlet flow distortion using relatively less computational cost. A full-annular two-dimensional (2D) optimization approach which optimizes vane blades on a full-annular section plane at different radial locations, and a partial-annular three-dimensional (3D) optimization method which just considers the vane blade in the distortion region, are developed based on the analysis of flow mechanism in the compressor. Effects of feasible designs on the aerodynamic performance including efficiency, total pressure ratio, stall margin and blade row loss are studied correspondingly. The purpose is to further tap the potential of non-axisymmetric vane to satisfy the requirements of high-efficiency and wide stall margin for compressors of modern and next-generation gas turbine engines.

2. Compressor Studied and Numerical Simulation Method

The compressor investigated in this paper is the inlet 1.5-stage of a pre-research commercial gas turbine compressor. It is composed of inlet guide vane (IGV), rotor and stator rows, and the number of these three blade rows is 42, 27 and 47, respectively. When operating in practice, the compressor endures inlet flow distortion due to the flow separation in its upstream lateral intake, as illustrated in Fig. 1. This flow non-uniformity cannot be totally eliminated only by optimizing the intake component, so the motivation of this work is to make the compressor adapt to this operating condition by redesigning the IGV. It may be worth noting that no experiments are available for this compressor at the present time, but the numerical simulation procedure will be introduced and validated based on other compressor models.

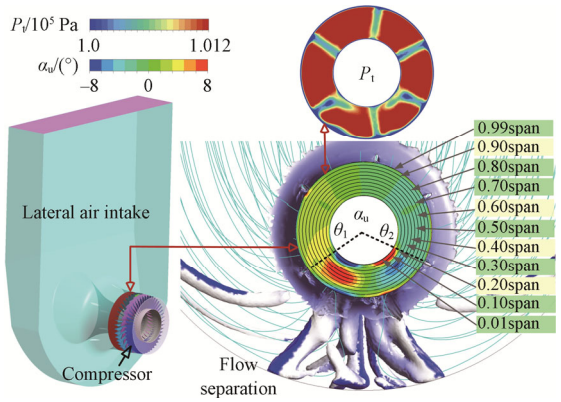

Fig. 1 Distorted inlet flow of the compressor due to flow separation in its upstream lateral air intake

2.1 General introduction of the numerical method

All numerical simulations in this work were conducted using ANSYS CFX [19] to solve the three-dimensional steady Reynolds-averaged Navier-Stokes (RANS) equations, which are expressed as:

$$\begin{cases} \dfrac{\partial \rho}{\partial t}+\dfrac{\partial}{\partial x_j}\left(\rho V_j\right)=0 \\ \dfrac{\partial\left(\rho V_i\right)}{\partial t}+\dfrac{\partial}{\partial x_j}\left(\rho V_i V_j\right)=-\dfrac{\partial P_s}{\partial x_i}+\dfrac{\partial}{\partial x_j}\left[\mu_{\text{eff}}\left(\dfrac{\partial V_i}{\partial x_j}+\dfrac{\partial V_j}{\partial x_i}\right)\right] \\ \dfrac{\partial\left(\rho h_{\text{tot}}\right)}{\partial t}-\dfrac{\partial P}{\partial t}+\dfrac{\partial}{\partial x_j}\left(\rho V_j h_{\text{tot}}\right)=\dfrac{\partial}{\partial x_j}\left(\lambda\dfrac{\partial T}{\partial x_j}+\dfrac{\mu_t}{Pr_t}\dfrac{\partial h_s}{\partial x_j}\right) \end{cases} \quad (1)$$

where the time relevant terms are retained since time-marching method is employed to get final steady-state solution. The entire flow was regarded as fully turbulent, and the Shear Stress Transport (SST) model was applied to predict the turbulence while no

transition criterion was invoked. Also, high resolution was chosen in the advection scheme.

Since there is no available experiment data for the compressor in Fig. 1, another in-house compressor (Compressor A) which has similar aerodynamic and geometric parameters was first simulated to examine the predictive accuracy of the CFD solver. To do this, a single-passage domain of Compressor A was constructed, as shown by Fig. 2(a), and structured meshes with a grid number of about four millions were generated. Then numerical simulations were performed. Uniform inlet total pressure ($P_{t,in}$) and total temperature ($T_{t,in}$) with axial inlet flow angle were set, and a medium turbulence intensity value of 5% was specified. Meanwhile, the outlet static pressure was continuously changed to get different mass flow conditions in experiments. All solid walls were managed using no-slip and adiabatic conditions with smooth wall roughness, while the lateral sides of the domain were set as periodic interface. The solution was deemed to be converged if residuals of the continuity and the momentum in three directions were less than 10^{-6} and 10^{-5} respectively.

Two parameters are used for performance evaluation in this paper. The first is total pressure ratio (π), defined as:

$$\pi = P_{t,out}/P_{t,in}, \quad \pi_n = \pi/\pi_{\eta\text{-peak}} \tag{2}$$

and the second is temperature rise or torque efficiency η, as formulated as:

$$\begin{cases} \eta = \dfrac{\pi^{(k-1)/k} - 1}{\theta_t - 1} & \text{or} \\ \eta = \dfrac{k}{k-1} R_g T_{t,in} \dfrac{m \cdot \left[\left(\dfrac{P_{t,out}}{P_{t,in}} \right)^{(k-1)/k} - 1 \right]}{2\pi NM/60}, \quad \eta_n = \dfrac{\eta}{\eta_{peak}} \end{cases} \tag{3}$$

where $\theta_t = T_{t,out}/T_{t,in}$; m is the mass flow; M is the torque; N is the blade number, and the subscript n indicates that all parameters are normalized using those at the peak efficiency condition respectively. Fig. 2(b) compares predicted total pressure ratio and torque efficiency under different mass flow rate conditions, and it implies that compared to experiments, the CFD solver used in this paper can predict similar characteristics of the compressor under uniform inflow. The efficiency predicted by CFD is slightly larger than experimental data, and this is because that the measured torque is composed of the part consumed by the compressor and the no-load running torque of the bearing. Since the no-load running torque is not precisely measured and cannot be subtracted when calculating the efficiency, the experimental data is smaller. Despite this, the CFD solver can offer a right evaluation on the compressor performance.

Considering numerical simulation method to evaluate the compressor performance under inlet distortion conditions, there have been developed various algorithms that own lower-fidelity but higher computational efficiency compared to unsteady full-annular calculation. Typical works include those using meanline calculation [20], streamline curvature approach [21], body-force method [23] and CFD with Fourier Transformation [24]. The first three methods [20–23] are worth further evaluating for adopting them to the optimization that will be introduced in Section 3, and the fourth [24] still need unsteady simulation that this paper does not consider at the present stage. Due to these reasons and in order to develop appropriate numerical method for later 2D and 3D non-axisymmetric IGV designs, two low-cost computation methods are first developed and they are described respectively as follows.

2.2 Numerical simulation method of full-annular 2D vane

To conduct full-annular 2D non-axisymmetric IGV design, the first issue needed to be clarified is whether using full-annular 2D vane domain can capture the similar flow field in 3D compressor. To clarify this

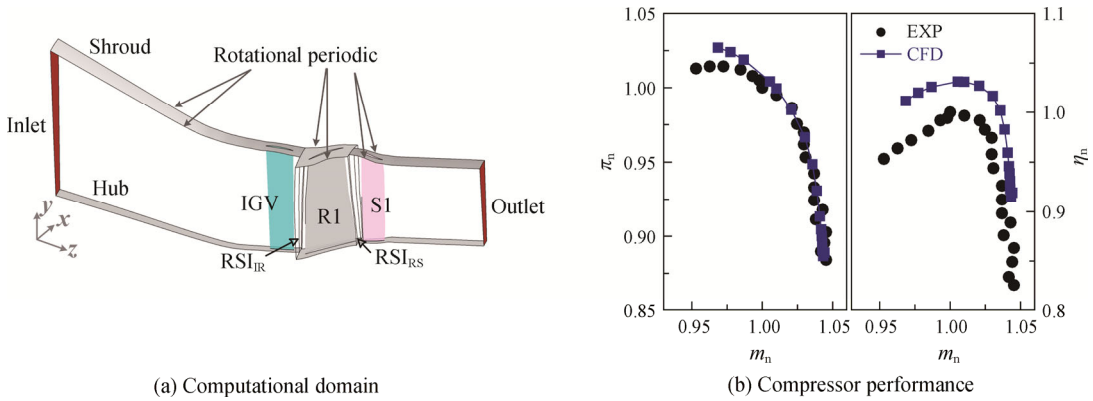

(a) Computational domain (b) Compressor performance

Fig. 2 Predicted performance of a 1.5-stage compressor

problem, numerical simulations are first conducted based on full-annular 3D vane and full-annular 2D vane sections at three span-normalized locations, as illustrated by the computational domains in Fig. 3. The grid number is 22 million and 3.5 million respectively. The RANS equation set in Eq. (1) is solved again, and the total pressure and swirl flow field shown in Fig. 1 is set as the inlet boundary condition for the two computational domain, while a constant static pressure is specified at the outlet. It should be mentioned that the outlet pressure for the 2D vane equals to the area-averaged pressure over the outlet of the 3D vane, and the upper and lower planes are specified as free-slip wall. Predicted contours of flow angle (α_u) across the IGV are compared in Fig. 4.

It can be observed from Fig. 4 that the largest difference is that swirl strength in 2D simulation is weaker than that in 3D results. This is because that the 2D simulation cannot consider the span-wise mixing of the distorted flow. Despite this, distributions of α_u predicted using full-annular 2D domain is generally similar to those using 3D model. Therefore, numerical simulations based on the 2D model will be further used for objective calculation in subsequent full-annular non-axisymmetric 2D IGV design.

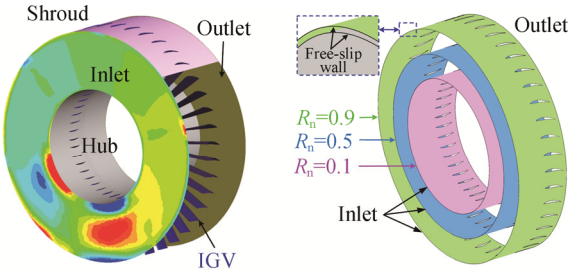

(a) Full-annular 3D model (b) Full-annular 2D model

Fig. 3 Computational domain of the IGV

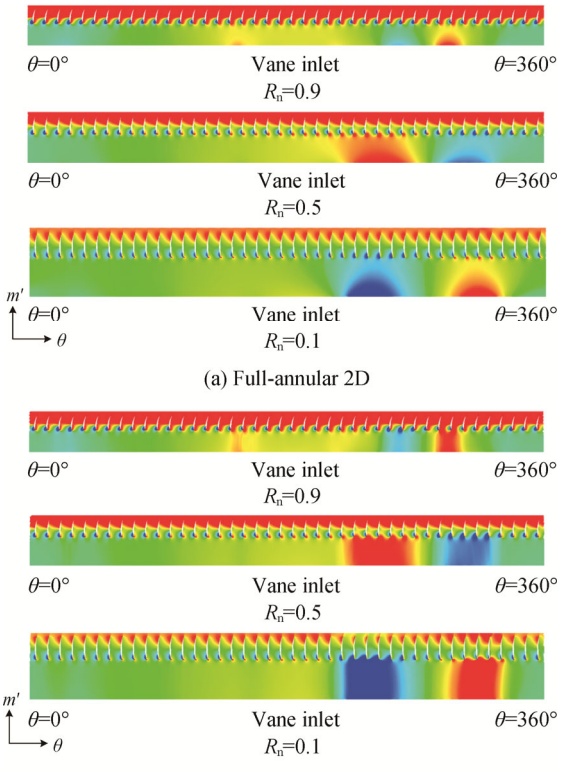

(a) Full-annular 2D

(b) Full-annular 3D

Fig. 4 Predicted contours of flow angle

2.3 Numerical simulation of partial-annular 3D compressor

The idea of conducting partial-annular 3D optimization first stems from an observation that high-intensity swirl distortion is mainly located at lower-radius region on the interface between lateral air intake and compressor, as indicated by θ_1 and θ_2 in Fig. 1. Also, using the above full-annular 2D vane cannot evaluate the compressor pressure ratio (π), efficiency (η) and the stall margin. On the other hand and as introduced in Section 1, conducting unsteady simulation to evaluate the compressor performance under inlet distortion is really unbearable for an optimization process, and hence efforts are focused on developing an appropriate steady CFD approach.

It is known that the key problem for steady-state RANS simulations lies in tackling the transmission of flow information on rotor-to-stator interface. One method is traditional and generally-used mixing-plane strategy, which transports the circumferentially averaged flow quantities across the interface, while the other one is frozen rotor, which transports real flow information to the next domain [23]. In order to further compare these two methods, performance of a two-stage compressor (Compressor B) is simulated. This compressor is a typical fan in a modern turbofan engine under uniform and distorted inflow being studied by the authors. For this two-stage compressor, steady CFD simulations are conducted again by solving the RANS equation set in Eq. (1). Structured mesh with a gird number of about 80 million is generated using NUMECA-AUTOGRID after a grid sensitivity study, and boundary condition settings are similar to those for calculating the performance of Compressor A (Fig. 2). In addition, the interface between the stationary inlet domain and the first-stage rotor domain is set as the frozen rotor (FR) interface and the mixing plane (MP) respectively, while other rotor-stator interfaces are defined using MP method. Predicted results are compared to experiments [25] in Fig. 5. Since this compressor is not mainly studied in this paper, a simple analysis is just presented here and it implies that results predicted by CFD with the MP interface are more consistent with the experiments than those with the FR interface. Deeper analysis is conducting by using sliding-mesh interface between rotor and stator domains, but this comparison in Fig. 5 suggests that the MP

interface can be adopted to evaluate compressor performance under inlet distortion.

Based on the above analysis, two 3D computational domains as shown in Fig. 6 are constructed. The first compressor model in Fig. 6(a) is composed of multiple IGV and rotor passages, and the frozen rotor method (Opt-FR) is adopted to transfer flow information between IGV and rotor. Compared to this, the second model in Fig. 6(b) just includes one rotor passage, and the mixing plane (Opt-MP) is specified at the IGV-to-rotor interface.

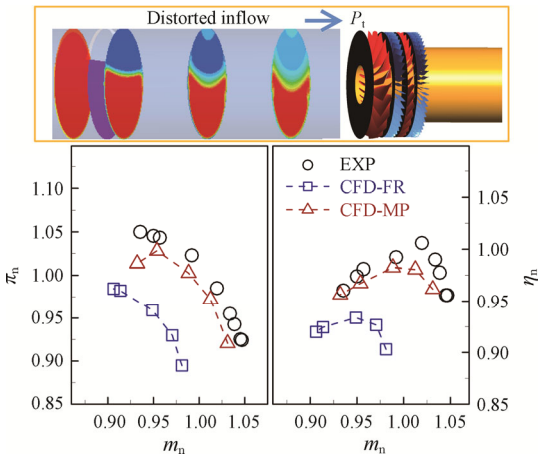

Fig. 5 Performance of a two-stage compressor under distorted inflow using CFD simulations with frozen rotor and mixing plane methods

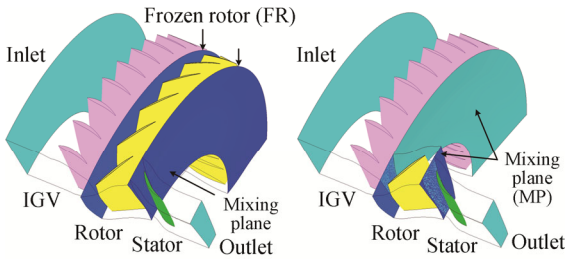

(a) Opt-FR (b) Opt-MP

Fig. 6 Computational domain for partial-annular 3D simulations

Meanwhile, only one stator passage is constructed for the two models, and the rotor-stator interface is set as mixing plane. It may be worth mentioning again that the purpose emphasizes more on qualitative evaluation of the performance with low-cost calculation than on accurate quantitative calculation at the design stage.

Using the computational models in Fig. 6, compressor characteristics under uniform inflow and distorted inflow in Fig. 1 are numerically simulated by solving the RANS equation set, and results are depicted in Fig. 7, where Fig. 7(a) first presents the results of a grid sensitivity study based on the uniform inflow condition. Three level of grid number, i.e., N_1, N_2 and N_3 are considered for gird generation. It can be seen that little change is induced when increasing the grid node number, and the middle number level (N_2) is employed. In addition, the legend of clean in Fig. 7 represents predicted performance of the compressor under uniform inflow condition, while Opt-FR and Opt-MP indicate that under inlet distortion but using the aforementioned two interface algorithms. It can be seen that deteriorations in π_n and η_n due to inlet total pressure and swirl distortion are predicted by both Opt-FR and Opt-MP methods, and the deterioration level for π is more intense when using the Opt-FR approach. Despite this, the peak efficiency and stall margin of the compressor under distorted inflow estimated is nearly the same between Opt-FR and Opt-MP simulations. Considering that hundreds of numerical simulation cases need be conducted during the optimization, the Opt-MP method will be adopted to evaluate the performance of partial-annular 3D design samples. Also, two mass flow rate conditions that will be set during the optimization. One ($m_{n,4}$) is the mass flow rate near the peak efficiency, while the other ($m_{n,5}$) is that near the stall condition.

Apart from total pressure ratio and efficiency, stall margin of the compressor is also considered during the partial-annular 3D optimization process. To determine an appropriate indicator of the stall margin, Fig. 8(a) first displays the contours of the axial velocity near rotor blade tip at different mass flow conditions (m_n, see

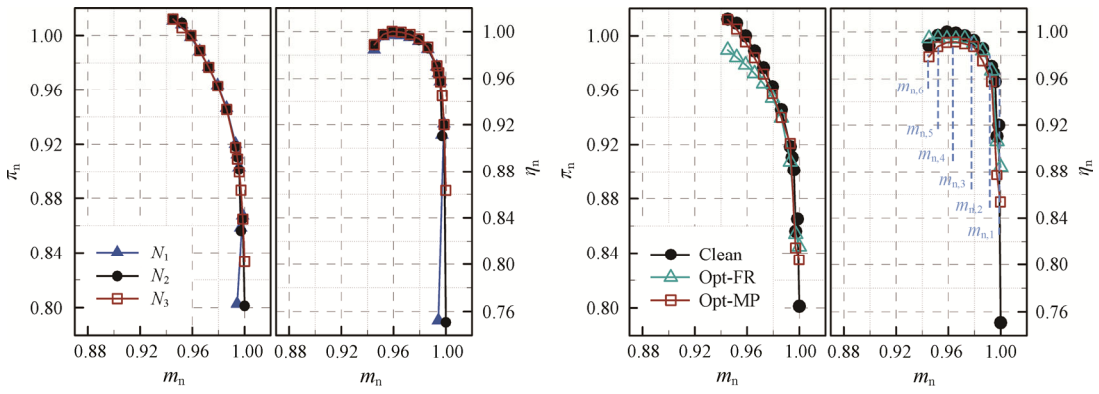

(a) Grid sensitivity study for clean case (b) Impact of different 3D domain

Fig. 7 Performance characteristics of the compressor

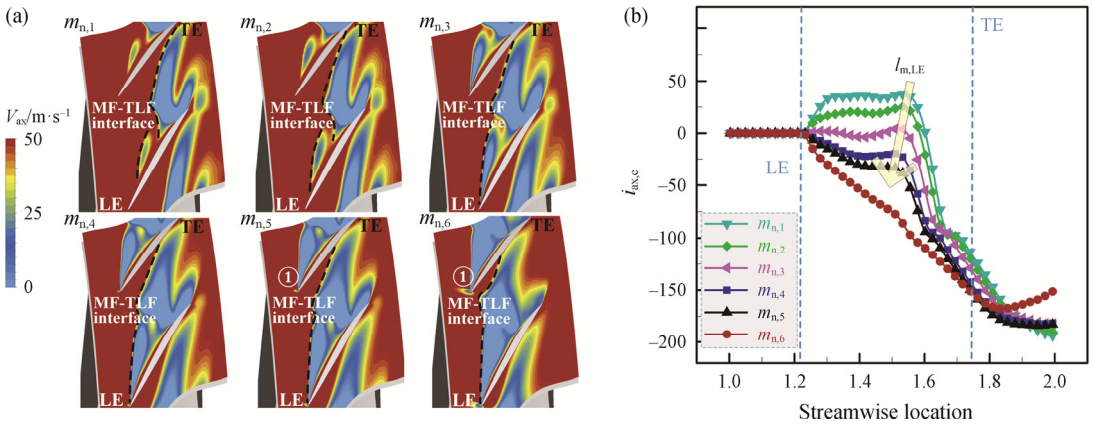

Fig. 8 Indicator for the surge margin (a) contour of V_{ax} near the blade tip, (b) $i_{ax,c}$

Fig. 7). It can be seen that the interface between main flow and tip leakage flow (MF-TLF interface) is pushed towards leading edge (LE) with the decrease in m_n. This indicates that this compressor encounters a spike-type stall process which is ascribed to the spillage of MF/TLF interface from LE. Fig. 8(b) shows the distributions of the accumulated axial momentum (i_{ax}) from rotor leading edge. It can be observed that with the increase in m_n, the peak value of i_{ax} is decreased and gradually migrated towards LE, which is consistent with the spillage process of MF/TLF interface from LE. Therefore, the peak value of i_{ax} for each design cases will be examined to evaluate effects of non-axisymmetric vane on compressor stall margin. Details of this axial momentum criterion can be referred to the previously published paper of the authors [26].

3. Design Optimization Method of Non-Axisymmetric Vane

The distorted inlet flow filed in Fig. 1 mainly presents two pairs of swirl generated by the flow separation in the lateral intake as flow cannot turn from radial direction to axial direction rigidly. Therefore, the first criterion of non-axisymmetric IGV design is to match this flow swirl by optimizing the vane blade leading edge metal angle ($\chi_{1,I,d}$, see Fig. 9), while the second is to adjust the vane trailing edge metal angle ($\chi_{2,I,d}$) to make the vane outlet flow consistent with the leading edge metal angle of downstream rotor ($\beta_{1,R,d}$). Other geometry parameters of the vane profile such as chord and thickness are also considered. Based on this design philosophy, a full-annular 2D and a partial-annular 3D optimization approaches are developed, and they are described in detail as below.

3.1 Inlet flow distortion pattern and parametrization

Prior to the description of the optimization procedure, a method to parameterize the inlet distortion is worth introducing. Fig. 1 implies that the flow swirl distortion spreads the whole compressor inlet plane, circumferential distributions of blade inlet angle distortions ($\chi_{1,dis}$= α_u–$\chi_{1,I,d}$) at 11 span normalized locations (R_n) are plotted in Fig. 9. In order to appropriately describe their feature, a parameterization approach is established based on the Fast Fourier Transform analysis [27] of $\chi_{1,dis}$. The relevant mathematical formulation of modified leading edge metal angle ($\chi_{1,I}$) can be expressed as:

$$\begin{aligned}\chi_{1,I} &= \chi_{1,I,d} + \chi_{1,distortion} \\ &= \chi_{1,I,d} + \sum_{k=1}^{l}\{c_k \cdot \cos[k\theta + \varphi_k]\}\end{aligned} \tag{4}$$

where c_k and φ_k are Fourier coefficients (also termed as amplitude and phase respectively) of k-th term of the Fourier modes, and the total number (l) of the modes is determined by that of raw data of $\chi_{1,dis}$.

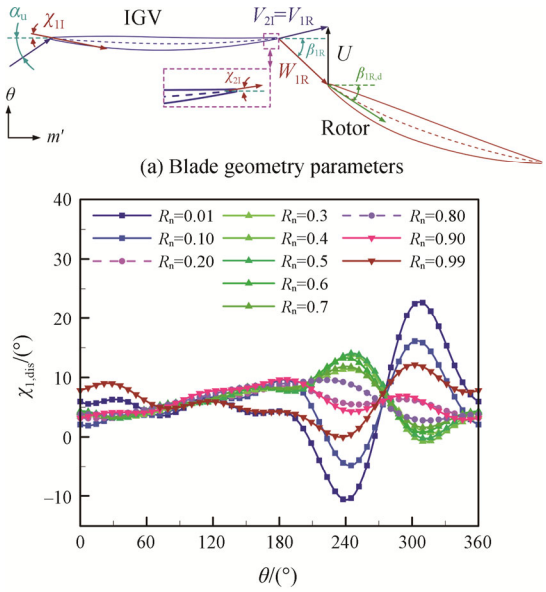

(a) Blade geometry parameters

(b) Circumferential distributions of $\chi_{1,dis}$

Fig. 9 Circumferential distributions of $\chi_{1,dis}$ at different radial location on the compressor inlet plane

According to Eq. (4), the data in Fig. 9 are reconstructed using different number of Fourier modes. Results indicate that when the mode number exceeds 5, the fitting error tends to be small, as shown by sums of five and six terms of the Fourier modes in Fig. 10 respectively. It can be seen that changing characteristics of $\chi_{1,\mathrm{dis}}$ along the circumferential direction can be demonstrated accurately based on the Fourier modes with l=5. This will support the full-annular 2D optimization in Section 3.2, and will be further discussed in Section 3.3.

3.2 Full-annular 2D optimization approach

The purpose of full-annular 2D optimization is to design geometrical parameters of vane blade profiles at different radial locations separately. Its mathematical description can be expressed as:

$$\begin{aligned}&\min f_1\left(\chi_{1,\mathrm{I}},\chi_{2,\mathrm{I}}\right)=C_{p,\mathrm{t,IGV}}\\&\min f_2\left(\chi_{1,\mathrm{I}},\chi_{2,\mathrm{I}}\right)=\max\left\|\beta_{1,\mathrm{R,d}}-\beta_{1,\mathrm{R},i}\right\|^2\end{aligned}\tag{5}$$

where two optimization objectives (f_1 and f_2) are considered to minimize the total pressure loss of inlet guide vane and the inlet incidence distortion of the rotor respectively. The parameter, $\beta_{1,\mathrm{R,itheta}}$, is leading ledge flow angle at rotor inlet, and it can be calculated using flow parameters at vane outlet via:

$$\beta_{1,\mathrm{R,itheta}}=\arctan\left(\frac{U_i-V_{\theta,i}}{V_{z,i}}\right)\tag{6}$$

where U_i is the rotating velocity of examined points along the circumferential direction at a radial location. $V_{\theta,i}$ and $V_{z,i}$ are the circumferential and axial velocity components respectively.

Two geometrical parameters, i.e., the leading edge and trailing edge metal angles ($\chi_{1,\mathrm{I}}$ and $\chi_{2,\mathrm{I}}$) of vane blade, are considered in the full-annular 2D optimization process. Their characteristics along the circumferential direction are parameterized using the Fourier modes, as formulated as:

$$\begin{aligned}\chi_{1,\mathrm{I}}&=\chi_{1,\mathrm{I,d}}+\chi_{1,\mathrm{distortion}}\\&=\chi_{1,\mathrm{I,d}}+\sum_{k=1}^{l=5}\left\{c_k\cdot\cos\left[k\theta+\varphi_k\right]\right\}\end{aligned}\tag{7}$$

$$\chi_{2,\mathrm{I}}=\chi_{2,\mathrm{I,d}}+b\cos\left(\theta+\psi\right)\tag{8}$$

It is worth mentioning that five terms of the Fourier modes are combined to parameterize $\chi_{1,\mathrm{I}}$ based on the analysis in Fig. 10, while only one term is used for parameterizing $\chi_{2\mathrm{I}}$ since the vane outlet flow field cannot be obtained in advance when $\chi_{1,\mathrm{I}}$ changes. Therefore, there are only twelve design variables for one full-annular 2D optimization at a specific span-normalized location (e.g., 0.50span in Figs. 1 and 2). This reduces the design freedom degree considerably compared to traditional blade design frame, which need optimize $2N_{\mathrm{IGV}}$ (N_{IGV} is the blade number of IGV) parameters.

Another innovative point of this paper lies in that not blade parameters in all radial locations are involved in the design process, but only seven span-normalized locations are considered. This is determined via two aspects of analysis. The first can be seen from Fig. 9 that distributions of $\chi_{1,\mathrm{dis}}$ can be divided into two categories, delimited by the radial locations of 0.2span and 0.8span. This means that characteristics of $\chi_{1,\mathrm{dis}}$ have the same feature from 0.01span to 0.2span (also, from 0.8span to 1.0span), and from 0.2span to 0.8span. The second can be interpreted by Fig. 11, where discrete points represent the Fourier coefficients of the first and second order of the Fourier modes obtained via FFT for $\chi_{1,\mathrm{dis}}$ at 11 span-normalized locations (0.01span to 0.99span). Two lines as labeled by fit-11 and fit-07 are plotted via polynomial curves fitting based on 11 and 7 points respectively. It can be seen that the fit-07 curve can represent the overall changing trend of each Fourier coefficient in the radial direction. Considering these two aspects, full-annular circumferential distribution of $\chi_{1,\mathrm{I}}$ and $\chi_{2,\mathrm{I}}$ at seven span-normalized locations are optimized

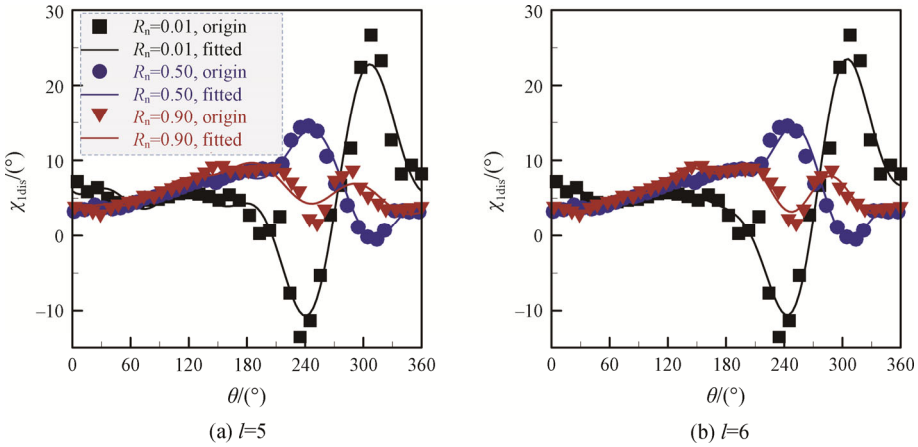

(a) l=5 (b) l=6

Fig. 10 Parameterization of $\chi_{1\mathrm{dis}}$ using 5 and 6 terms of the Fourier modes

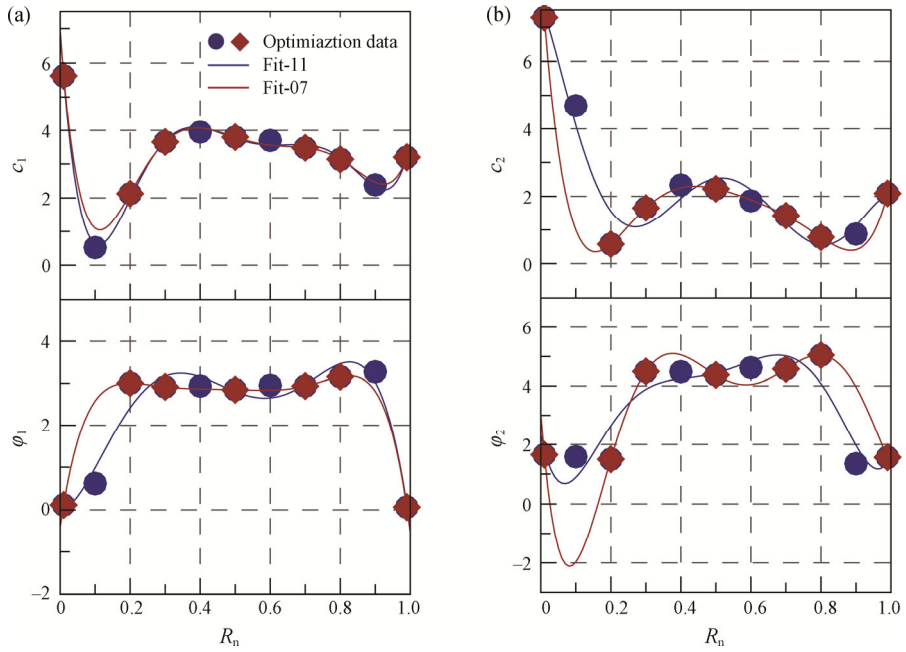

Fig. 11 Polynomial fitting of the Fourier coefficients using data at 11 and 7 radial locations

in current design stage. All of the considerations aid to further alleviate the design workload and cost.

3.3 Partial-annular 3D optimization approach

As mentioned in the analysis of Figs. 7 and 8, the purpose of partial-annular 3D design is to optimize the compressor performance including total pressure ratio, efficiency and stall margin via adjust geometrical parameters of vane in distortion region. The corresponding mathematical formulation is:

$$\begin{aligned} &\max \eta\left(\chi_{1,\mathrm{I}}, \chi_{2,\mathrm{I}}, b_{\mathrm{I}}, t_{\mathrm{I,max}}\right) \\ &\max \pi\left(\chi_{1,\mathrm{I}}, \chi_{2,\mathrm{I}}, b_{\mathrm{I}}, t_{\mathrm{I,max}}\right) \\ &\max \mathrm{SMI}\left(\chi_{1,\mathrm{I}}, \chi_{2,\mathrm{I}}, b_{\mathrm{I}}, t_{\mathrm{I,max}}\right) \end{aligned} \tag{9}$$

where design parameters also includes chord (b_{I}) and maximum thickness ($t_{\mathrm{I,max}}$) of vane blade profiles, and SMI implies stall margin improvement.

Fig. 12 plots local distributions of inlet swirl along the circumferential direction at three span-normalized locations. The FFT analysis is conducted again, and results indicate that using two terms of Fourier modes can characterize the local distortion feature. Therefore, circumferential distributions of leading-edge metal angle are parameterized by:

$$\begin{aligned} \chi_{1,\mathrm{I}} &= \chi_{1,\mathrm{I,d}} + \chi_{1,\mathrm{distortion}} \\ &= \chi_{1,\mathrm{I,d}} + \sum_{k=1}^{l=2}\left\{c_k\left(R_{\mathrm{n}}\right)\cdot\cos\left[y(\theta)+\varphi_k\left(R_{\mathrm{n}}\right)\right]\right\} \end{aligned} \tag{10}$$

It is worth emphasizing that the Fourier coefficients in Eq. (10) are further parameterized. They are expressed as function in terms of radius using trigonometric series:

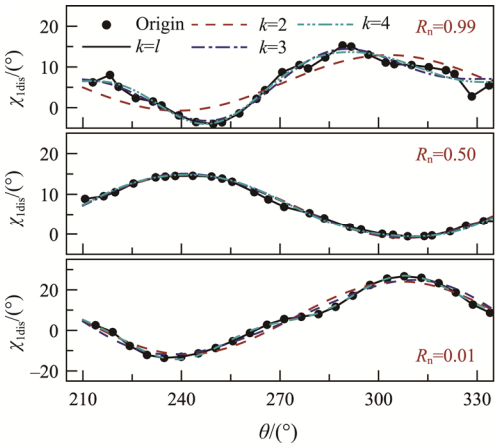

Fig. 12 Distributions of $\chi_{1\mathrm{dis}}$ in the distortion region

$$\begin{aligned} c_k &= a_{c,0,k} + a_{c,\mathrm{F1},k}\cos\left(w_{c,k}R_{\mathrm{n}}\right) + b_{c,\mathrm{F1},k}\sin\left(w_{c,k}R_{\mathrm{n}}\right) \\ \varphi_k &= a_{\varphi,0,k} + a_{\varphi,\mathrm{F1},k}\cos\left(w_{\varphi,k}R_{\mathrm{n}}\right) + b_{\varphi,\mathrm{F1},k}\sin\left(w_{\varphi,k}R_{\mathrm{n}}\right) \end{aligned} \tag{11}$$

where a, b and ω will be regarded as optimization variables. Based on Eqs. (10) and (11), the distribution of $\chi_{1,\mathrm{I}}$ in both circumferential and radial directions can be described using only twelve parameters.

Moreover, the other three design variables, i.e., trailing edge metal angles ($\chi_{2,\mathrm{I}}$), chord (b_{I}) and maximum thickness ($t_{\mathrm{I,max}}$) are defined using two modes of Fourier modes (the last number F1, F2 in subscript):

$$\begin{aligned} \chi_{2,\mathrm{I,R}} &= \chi_{2,\mathrm{I,d,R}} + c_{\chi_{2,\mathrm{I,R,F1}}}\cos\left[(\theta-\theta_0)+\psi_{\chi_{2,\mathrm{I,R,F1}}}\right] \\ &\quad + c_{\chi_{2,\mathrm{I,R,F2}}}\cos\left[(\theta-\theta_0)+\psi_{\chi_{2,\mathrm{I,R,F2}}}\right] \end{aligned} \tag{12}$$

$$b_{\mathrm{I,max,R}} = b_{\mathrm{I,d,R}} + c_{b_{\mathrm{I,R,F1}}} \cos\left[(\theta-\theta_0)+\psi_{b_{\mathrm{I,R,F1}}}\right] + c_{b_{\mathrm{I,R,F2}}} \cos\left[(\theta-\theta_0)+\psi_{b_{\mathrm{I,R,F2}}}\right] \quad (13)$$

$$t_{\mathrm{I,max,R}} = t_{\mathrm{I,d,R}} + c_{t_{\mathrm{I,R,F1}}} \cos\left[(\theta-\theta_0)+\psi_{t_{\mathrm{I,R,F1}}}\right] + c_{t_{\mathrm{I,R,F2}}} \cos\left[(\theta-\theta_0)+\psi_{t_{\mathrm{I,R,F2}}}\right] \quad (14)$$

According to the above introduction, it can be concluded that twenty-four variables will be involved for later partial-annular 3D non-axisymmetric vane optimization. If using traditional blade optimization method and the chord, the maximum thickness, the inlet and outlet angles of blade profiles at 11 radial locations are designed, and there will be 44 variables for axisymmetric blade and $44N_{\mathrm{IGV}}$ for non-axisymmetric design. Therefore, the method proposed here is very valuable for engineering design as it reduces the degree of design freedom dramatically.

3.4 Optimization algorithm

To solve the full-annular 2D and partial-annular 3D optimization problems in Eqs. (5) and (9) respectively, an in-house generical algorithm (GA) integrated with design of experiment (DOE) and response surface (RS) method is adopted [28]. The corresponding optimization flow-chart is shown in Fig. 13. The first step is to produce a sample database, and this is finished via Latin Hypercube Sampling method. Aerodynamic performance of the full-annular 2D vane and partial-annular 3D compressor with these design samples are evaluated using the numerical simulation schemes in Sections 2.2 and 2.3 respectively. These samples are then employed to create Kriging RS model, and they are also regarded as the initial parent population for GA solution.

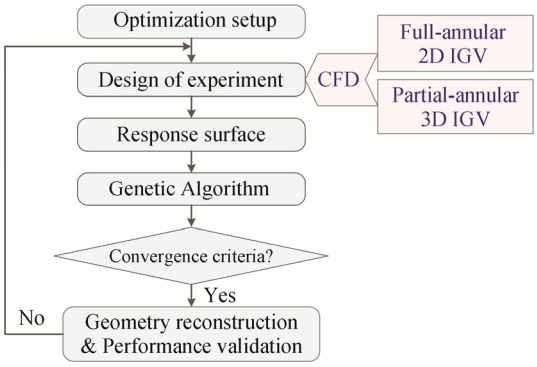

Fig. 13 Optimization flow-chart

The GA module invokes the RS model to calculate the fitness function according to the magnitude of objective functions and design constraints. Based on this, offspring populations are generated via executing selection, crossover, mutation and recombination operators. The probability of crossover and mutation is user-defined, and it is 0.9 and 0.1 for the current design respectively. If the optimization cannot satisfy the convergence criteria, more design samples are produced according to the infilling strategy based on expected improvement function. Then the above steps including performance evaluation, RS model generation and GA processing are carried out again. At the end of the optimization, a solution termed as Pareto-optimal front is finally obtained. It offers an analyzing perspective and choosing space to determine final designs.

4. Effects of Non-Axisymmetric Vane on Compressor Performance

4.1 Full-annular two dimensional optimization results and discussion

4.1.1 Optimization results

Based on the optimization strategy introduced in the former section, full-annular non-axisymmetric 2D vane profiles at seven radial locations are optimized. Fig. 14 presents the performance data of each design samples at the location of R_{n} being 0.3. It can be seen that a pareto-front associated with the two objectives is generated, and feasible designs are obtained after two rounds of optimization. Both the total pressure loss of the vane passage (f_1) and the flow non-uniformity at the vane outlet (f_2) are reduced. Schematic diagram of the profile for a feasible vane is also shown in Fig. 14.

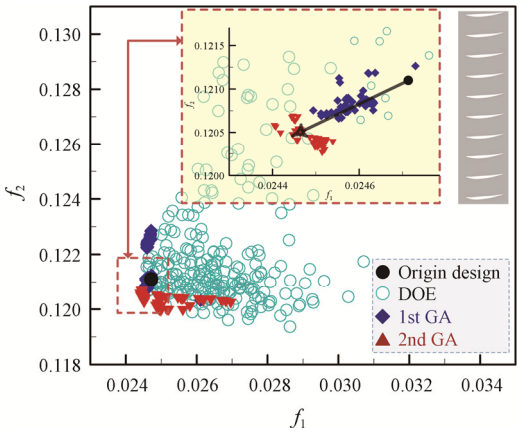

Fig. 14 Pareto-front of the partial-annular 2D IGV optimization, R_{n}=0.03

4.1.2 Reconstruction strategy and performance of three-dimensional non-axisymmetric vane

The full-annular optimization is conducted for 2D vane profiles at seven radial locations. In order to reconstruct 3D vane, two interpolation methods are employed. The first (OPT-1) is to conduct polynomial fitting based on the optimized data of five pairs of

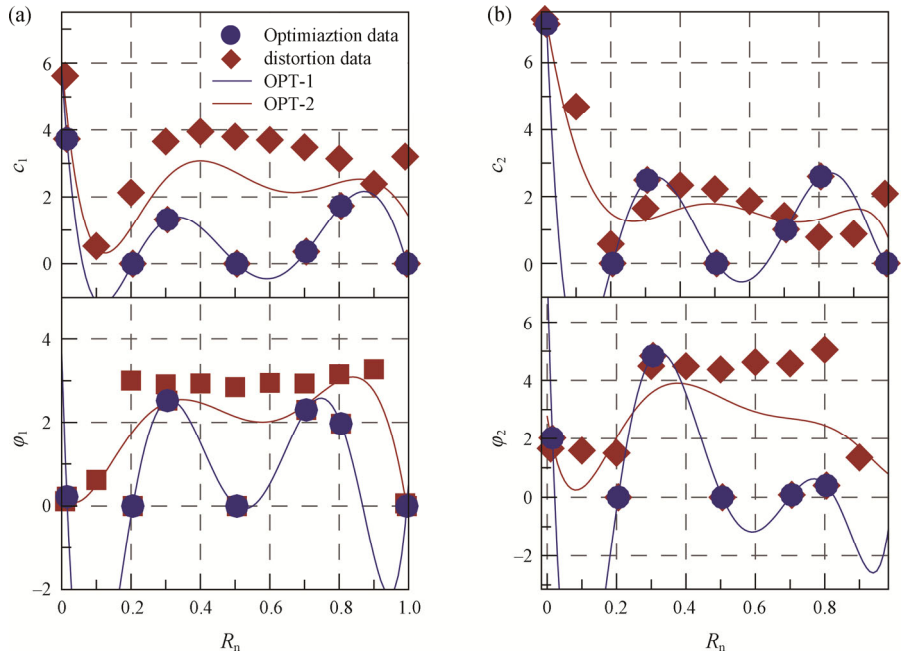

Fig. 15 Schematic diagram of reconstruction strategy for 3D non-axisymmetric IGV

Fourier coefficients at the examined seven locations, while the second fitting procedure (OPT-2) is based on both optimized data and the raw Fourier coefficients of inflow distortion data. Fig. 15 shows schematic diagrams of these two fitting methods for Fourier coefficients of the first two terms in the Fourier modes.

Based on the reconstructed 3D non-axisymmetric vane, numerical simulations are conducted to investigate the vane performance. Fig. 16 compares the total pressure loss across the original and two optimized vane passage, and the computational domain under distorted inflow condition is also shown. It can get two conclusions from the figure. One is that both two reconstructed 3D non-axisymmetric vane can lower the loss for all mass flow rate conditions; the other is that the second reconstructed geometry (OPT-2) that considers contributions of raw swirl distortion feature has lower loss than OPT-1.

In order to further assess the effects of full-annular non-axisymmetric vane on compressor performance, the OPT-2 design is coupled with original rotor and stator. Numerical simulations are then conducted to predict the compressor characteristic by solving the RANS equations under distorted inflow field in Fig. 1. Different outlet static pressure values are set to get the operating mass-flow conditions. Relevant computation domain and predicted compressor performance are presented in Fig. 17. Using the non-axisymmetric vane gets positive effects not only for total pressure ratio and efficiency, but also for compressor stall margin. However, the improvement in π and efficiency η is small when compared to the original geometry. This is mainly

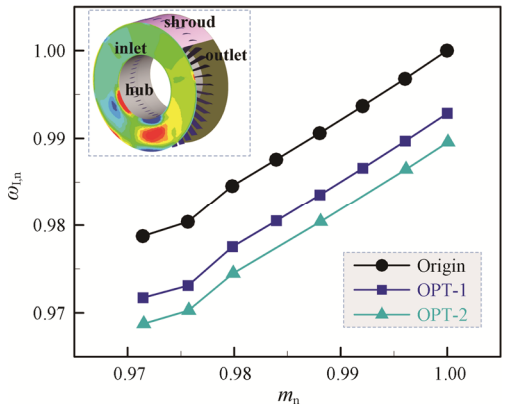

Fig. 16 Effects of non-axisymmetric IGV on total pressure loss of vane passage

because using non-axisymmetric vane changes the internal flow field in downstream rotor and stator, and hence may balance out the decrease in the total pressure loss across the vane passage.

4.2 Partial-annular three dimensional optimization result

One-round loop of the partial-annular 3D optimization is conducted in current stage, but it involves five hundred samples for each of the two mass flow rate conditions respectively. Fig. 18 first presents the overall performance of the design samples under the two mass flow conditions. The parameter, $l_{m,LE}$, indicates the streamwise location of the maximum $i_{m,LE}$ as shown in Fig. 8(a), and larger $l_{m,LE}$ implies that the MF-TLF interface is farther away from LE.

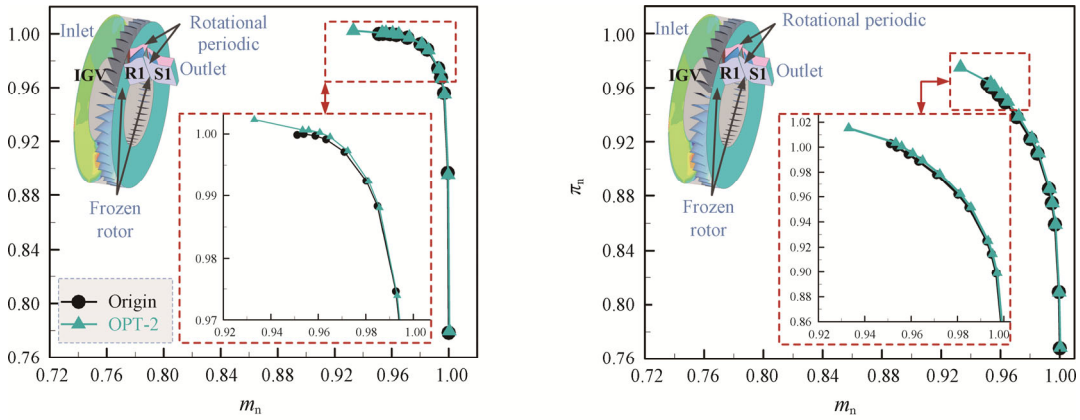

(a) Total pressure ratio (b) Efficiency

Fig. 17 Effects of non-axisymmetric vane on compressor performance

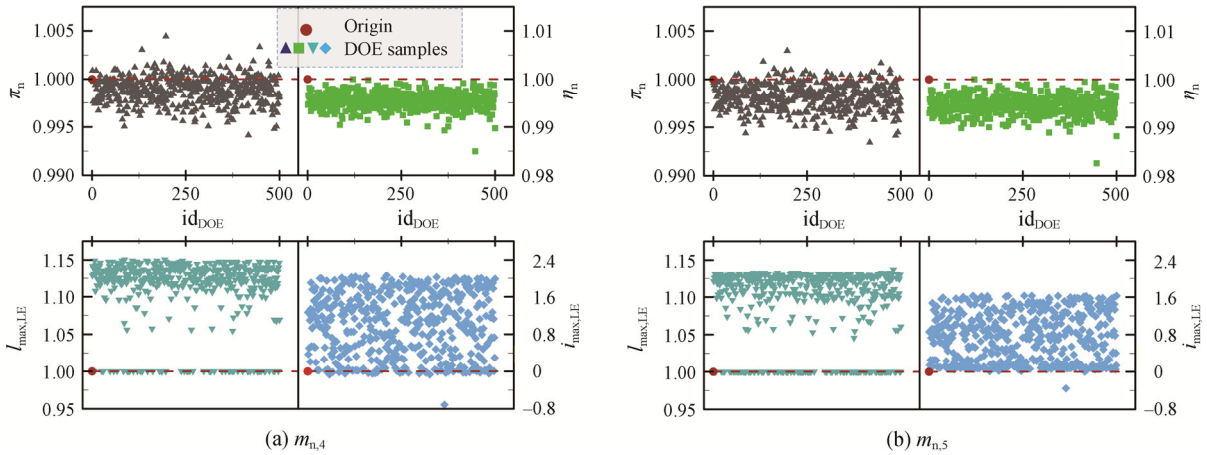

(a) $m_{n,4}$ (b) $m_{n,5}$

Fig. 18 Overall performance of partial 3D design samples

Fig. 18 first demonstrates a positive result that both total pressure ratio (π_n) and stall margin ($i_{m,LE}$ and $l_{m,LE}$) can be enlarged by some non-axisymmetric vane designs, while it also shows a negative result of slight deterioration in η_n by most of design samples. To further demonstrate the latter phenomenon, Fig. 19 plots design samples which have higher total pressure ratio and wider stability than origin design at the two mass-flow working conditions. It displays the decrease in the efficiency more clearly. These results differ from conclusions obtained in other research studies where the non-axisymmetric vane design is to improve compressor efficiency by decreasing the total pressure loss generated in the vane passage. In addition, Fig. 19 also indicates that the total pressure ratio can be increased at the near-stall condition ($m_{n,5}$); also, the ability of the compressor to resist instability can be enhanced since the value of $i_{max,LE}$ is larger than 1.

In order to further analyze the efficiency decay of the design samples, the total pressure loss of each blade row is plotted in Fig. 20, where the blade total pressure loss is defined as:

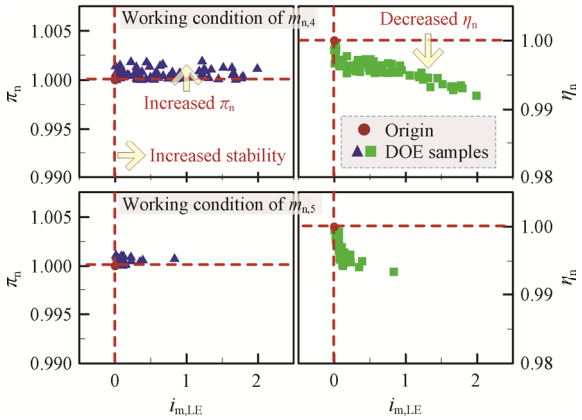

Fig. 19 Optimized vane with higher pressure ratio and stability than origin design

$$\omega_{I/S} = \frac{P_{t,in,I/S} - P_{t,out,I/S}}{P_{t,in,I/S} - P_{s,in,I/S}} \tag{15}$$

$$\omega_R = \frac{P_{tw,out,R,is} - P_{tw,out,R}}{P_{tw,in,R} - P_{s,in,R}}, \quad \frac{P_{tw,out,R,is}}{P_{tw,out,R}} = e^{\Delta s/R_g} \tag{16}$$

for the inlet guide vane (I) or stator (S) and the rotor (R) blade rows respective. The variable Δs in Eq. (16) is the entropy change across the rotor, and R_g is gas constant. These two parameters are used for calculating the isentropic total pressure at rotor blade out. The subscript n means that all loss values are normalized by the total pressure loss of each blade row in the original compressor respectively. It should be mentioned that only DOE designs having lower ω_I than the original vane are presented in Fig. 20. The comparison indicates that even though the total pressure loss of the IGV is decreased using the non-axisymmetric design, while that of the rotor and stator is increased. This is due to a fact that the non-axisymmetric design can influence the flow matching condition of downstream blade rows, and hence the efficiency is slightly reduced, as indicated by Fig. 18. More CFD simulations will be conducted for other mass flow conditions to analyze the whole characteristics of the compressor after the non-axisymmetric design. Despite this, the contour of $\omega_{I,n}$ in Fig. 20 indicates that the designed non-axisymmetric vane can match the distorted inflow and hence inhibit the flow separation near the blade surface.

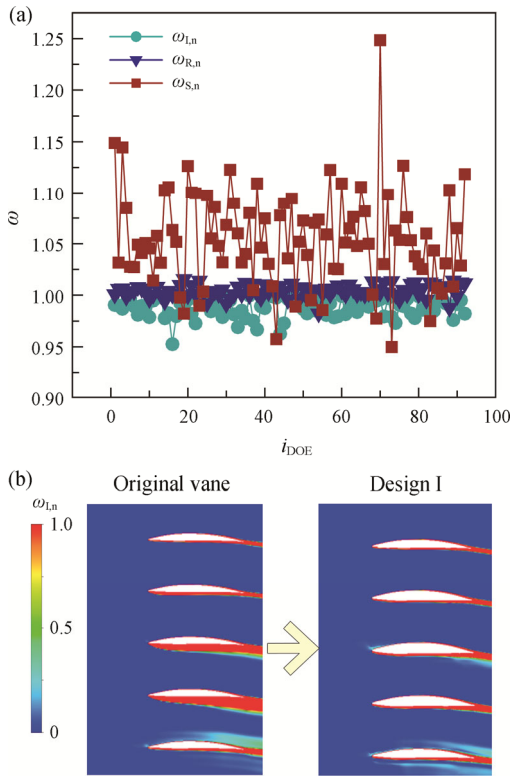

Fig. 20 Effects of blade row loss on compressor efficiency

5. Conclusions

Non-axisymmetric vane or stator design is a potential technique to match inlet flow distortion for compressor of both aircraft and industrial gas turbine engines. The main contribution of this article is establishing a full-annular 2D and partial-annular 3D optimization methods for non-axisymmetric vane design using relatively less computational cost. Numerical simulations based on different vane or compressor models are conducted to evaluate their aerodynamic performance. Typical conclusions are summarized as below.

(1) A full-annular 2D optimization and a partial-annular 3D optimization system are established considering the balance between appropriate evaluation on compressor performance under inlet distortion and computational cost. Also, a reconstruction method to create 3D non-axisymmetric vane base on the former method is developed, while a numerical simulation approach using multiple-passage vane and single-passage rotor and stator are integrated in the 3D optimization. These relatively low computational costs may aid to push the non-axisymmetric design into industrial application.

(2) A parametric method of inlet swirl angle is further developed by adopting the Fourier modes. It can describe the distortion pattern not only across the full-annular circumferential range but also in the radial direction.

(3) The designed non-axisymmetric vane based on full-annular 2D optimization successfully decreases the total pressure loss of vane passage under inlet distortion, while the designed vane using partial-annular 3D optimization has abilities to decrease the loss or improve compressor stall margin. Further analysis need to be conducted to clarify the tradeoff criterion.

Acknowledgements

The authors gratefully acknowledge the support of the National Science and Technology Major Project (J2019-II-0017-0038), the National Natural Science Foundation of China (NSFC 52206061) and Science Center for Gas Turbine Project (P2022-A-II-002-001).

Conflict of Interest

DU Juan is an editorial board member for Journal of Thermal Science and was not involved in the editorial review or the decision to publish this article. All authors declare that there are no competing interests.

References

[1] Sun D., Li Z., Dong X. Sun X., Calibration of S-duct swirl distortion based on vortex identification methods. Journal of Thermal Science, 2022, 31(1): 35–46.

[2] Saravanamuttoo H.I.H., Rogers G.F.C., Cohen H., Straznicky P.V., Gas turbine theory, Sixth Edition,

Pearson College Div Publisher, 2008.

[3] Pearson H., McKenzie A.B., Wakes in axial compressors. Journal of the Royal Aeronautical Society, 1959, 63: 415–416.

[4] Reid C., The response of axial flow compressors to intake flow distortion. Proceedings of the ASME 1969 Gas Turbine Conference and Products Show, Ohio, USA 1969.

[5] Stenning A.H., Inlet distortion effects in axial compressors. Journal of Fluids Engineering, 1980, 102(1): 7–13.

[6] Lesser A., Niehuis R., Transonic axial compressors with total pressure inlet flow field distortions. Proceedings of the ASME Turbo Expo 2014, Düsseldorf, Germany, 2014.

[7] Liu Y., Li J., Du J., Zhang H., Nie C., Stall warning strategy based on fast wavelet analysis in a multistage axial flow compressor. ASME Journal of Engineering Gas Turbines and Power, 2022, 144(4): 044501.

[8] Sun P., Gao H., Zhong J., Yang M., Study on the influence of total pressure distortion on end wall flow field in a supersonic compressor. Proceedings of the ASME Turbo Expo 2013, San Antonio, Texas, USA, 2013.

[9] Ramakrishna P.V., Govardhan M., Stall characteristics and tip clearance effects in forward swept axial compressor rotors. Journal of Thermal Science, 2009, 18(1): 40−47.

[10] Powrie H., Novis A., Gas path debris monitoring for F-35 Joint Strike Fighter propulsion system PHM. 2006 IEEE Aerospace Conference, Big Sky, USA, 2006.

[11] Gunn E.J., Hall C.A., Aerodynamics of boundary layer ingesting fans. Proceedings of the ASME Turbo Expo 2014, Düsseldorf, Germany, 2014.

[12] Davis M., Beale D., Sheoran Y., Integrated test and evaluation techniques as applied to an inlet swirl investigation using the F109 gas turbine engine. Proceedings of the ASME Turbo Expo 2008, Berlin, Germany, 2008.

[13] Dong X., Sun D., Li F., Jin D., Gui X., Sun X., Effects of stall precursor-suppressed casing treatment on a low-speed compressor with swirl distortion. ASME Journal of Fluids Engineering, 2018, 140(9): 091101.

[14] Davis M., Hale A., A parametric study on the effects of inlet swirl on compression system performance and operability using numerical simulations. Proceedings of the ASME Turbo Expo 2007, Montreal, Canada, 2007.

[15] Hall D.K., Analysis of civil aircraft propulsion with boundary layer ingestion. Ph.D thesis, Massachusetts Institute of Technology, 2015.

[16] Gunn E.J., Hall C.A., Nonaxisymmetric stator design for boundary layer ingesting fans. Journal of Turbomachinery, 2019, 141(7): 071010.

[17] Lu H.N., Yang Z., Pan T.Y., Li Q.S., Non-uniform stator loss reduction design strategy in a transonic axial-flow compressor stage under inflow distortion. Aerospace Science and Technology, 2019, 92: 347–362.

[18] Kumar S., Turner M.G., Siddappaji K., Celestina M., Aerodynamic design system for non-axisymmetric boundary layer ingestion fans. Proceedings of the ASME Turbo Expo 2018, Oslo, Norway, 2018.

[19] ANSYS Inc., ANSYS CFX-Solver theory guide, Release 15.0. Canonsburg: ANSYS Inc, 2013.

[20] Menegozzo L., Benini E., Meanline calculation of surge margin loss due to inlet flow distortion. Proceedings of the ASME Turbo Expo 2020, Virtual, Online, 2020.

[21] Pachidis V., Pilidis P., Templalexis I., Alexander T., Kotsiopoulos P., Prediction of engine performance under compressor inlet flow distortion using streamline curvature. Journal of Engineering for Gas Turbines and Power, 2007, 129(1): 97–103.

[22] Lobo B., Zori L., Galpin P., Holmes W., Efficient modeling strategy of an axial compressor fan-stage under inlet distortion. Proceedings of the ASME Turbo Expo 2016, Seoul, South Korea, 2016.

[23] Mehdi A., Effect of swirl distortion on gas turbine perability. PhD Thesis, Cranfield University, 2014.

[24] Guo J., Hu J., Wang X., Tu B., Efficient modeling of an axial compressor with swirl distortion. Journal of Thermal Science, 2021, 30(4): 1421–1434.

[25] Li Y., Li J., Du J., Liu Y., Zhang M., Zhang H.W., Optimized casing treatment to improve stall margin under circumferential pressure distortion in a high-speed axial flow fan. Proceedings of the ASME Turbo Expo 2023, Massachusetts, USA, 2023.

[26] Du J., Liu L., Nan X., Lin F., Chen J., Nie C., The dynamics of prestall process in an axial low-speed compressor with single circumferential casing groove, Proceedings of the ASME Turbo Expo 2013, San Antonio, USA, 2013.

[27] Peacock J.A., Fourier analysis. Scientific lecture, 2013. https://www.roe.ac.uk/japwww/teaching/fourier/fourier_lectures_part1.pdf

[28] Ba D., Zhang Q., Du J., Li Z., Zhang H., Nie C., Design optimization of axial slot casing treatment in a highly-loaded mixed-flow compressor. Aerospace Science and Technology, 2020, 107: 106262.